Int. J. Nonlinear Anal. Appl.
Volume 12, Special Issue, Winter and Spring 2021, 519-540
ISSN: 2008-6822 (electronic)
https://dx.doi.org/10.22075/ijnaa.2021.23992.2647

A computational study on aerodynamic characteristics of a simplified high-speed train: The effects of crosswinds and surface roughness

Alireza Hajipour, Arash Mirabdolah Lavasani*, Mohammad Eftekhari Yazdi

Department of Mechanical Engineering, Central Tehran Branch, Islamic Azad University, Tehran, Iran.

Abstract

The airflow around a simplified train model is investigated using a three-dimensional $\gamma - \widetilde{Re}_{\theta t}$ transitional approach. Four different yaw angles ($\theta = 10°, 20°, 30°$, and $40°$) perpendicular to the body of the simplified train model are considered which the magnitude of front air-flow is constant, and the magnitude of crosswind determines by yaw angle. The main aim of the research is to investigate the influences of the yaw angle and roughness on the time-averaged flow structure, turbulent quantities such as turbulent kinetic energy, dissipation rate, and the aerodynamic forces such as skin friction and pressure coefficients. The findings show that the yaw angle has a pronounced influence on the three-dimensional flow structure around the high-speed train. As the yaw angle augments, the aerodynamic forces like skin friction and pressure coefficients increase. Furthermore, the roughness has a negligible effect on the pressure coefficient. Also, the skin friction coefficient locally increases in the rough train body.

Keywords: High-speed train, Crosswind effects, Yaw angle, Surface roughness, $\gamma - \widetilde{Re}_{\theta t}$ transitional model.

1. Introduction

In recent years, many investigations have been performed around train aerodynamic, which shows a significant trend toward high-speed trains. Recent publications can conclude it carried out by Catanzaro et al. [1], Hemida and Krajnović [2], Baker et al. [3], Fragner et al. [4], García [5], Baker [6], Diasinos et al. [7], Paz et al. [8], Li et al. [9], Xia et al. [10]. One of the primary analyses

*Corresponding author

Email addresses: alirezahajipour@gmail.com (Alireza Hajipour), arashlavasani@iauctb.ac.ir (Arash Mirabdolah Lavasani), moh.eftekhari_yazdi@iauctb.ac.ir (Mohammad Eftekhari Yazdi)

Received: June 2020 *Revised:* January 2021

in the design process, which must be performed is the crosswind effects to improve the safety and efficiency of high-speed trains. As such, the aerodynamic design and optimization must be considered comprehensively due to increased stability and security, reducing energy consumption, acoustic noise, and improving operational convenience and comfort.

The crosswind plays an essential role in imposing aerodynamic force on high-speed trains during cruising in strong crosswinds. The analysis of crosswind effects in the designing process of the high-speed trains is so essential to improve the rollover stability and prevent the high risk of derailment or overturning because this kind of train is characterized by lightweight, which makes the aerodynamic forces considerable. In this context, many research types have been carried out to study different parameters of the high-speed trains subjected to strong crosswinds. It is worth to mention that the investigations have consisted of experimental works such as Copley [11], Chiu and Squire [12], Chiu [13], Hoppmann et al. [14], Suzuki et al. [15], and Baker et al. [3] are the researchers who carried out some experimental works on crosswind influences and computational analysis like Diedrichs [16], Hemida et al. [17], Khier et al. [18]. Kheir et al. [18] analyzed the high Reynolds number fluid flow over a simplified train. García et al. [19] numerically investigated the aerodynamic specification of a full-scale high-speed train subjected to crosswind. They characterized the fluid flow using the Large Eddy Simulation (LES) Method with commercial code ANSYS-Fluent. The influences of smooth and rough surfaces on different governing parameters such as flow structure and pressure coefficient are presented. Furthermore, the synthetic crosswind is defined using Turbsim software and based on the Kaimal spectrum. They compared the experimental and numerical findings of a fixed small-scale model. It is observed that the aerodynamic forces are higher for the train with a rough surface than a smooth one. Also, compared to rough and smooth walls, the suction peaks increase as the distance from the nose tip increases. It should be noted that other flow visualizations such as instantaneous flow structure and streamlines have similar reaction along the high-speed train body. Zhuang and Lu [20] investigated the aerodynamic of a high-speed train under the condition of crosswinds. They analyzed the instantaneous and time-averaged flow structure, turbulent statistics, and aerodynamic coefficient under the influence of crosswinds with different yaw angles using the LES model. The spectral analysis showed that several energetic frequencies dominate the time-averaged aerodynamic forces. Hemida and Krajnović [2] investigated both the time-averaged and instantaneous flows around a simplified generic train model. They used LES and considered two various yaw angles and Reynolds numbers of $35°, 90°$, and $3 \times 10^5, 3.7 \times 10^5$. Their primary purpose was to analyze the effects of yaw angles and the nose shape of the train on the flow structure and its aerodynamics coefficients. They concluded that the three-dimensional flow from the train's nose has an impact on a region of a length of 3.5 train height from the tip. Baker et al. [3] measured the crosswind forces on trains experimentally. They obtained full-scale and wind tunnel experiments to analyze the time-averaged and unsteady forces and moments on trains. They concluded that the importance of simulating local roughness effects within the tunnel experiments compared the results of full scale and wind tunnel. Also, it was indicated that the quasi-steady effects must be considered in calculating force and moments of aerodynamic admittances. In another investigation, Baker [21] reviewed different work that analyzed the aerodynamic of high-speed trains in recent years. It was attempted to describe to nature of the flow field in fundamental terms and the fact that the primary cause of aerodynamic forces is the existence of flow filed. Different types of models from full scales to small scales that are tested in the wind tunnels and computational types of literature are gathered to draw a comprehensive view of the flow structure around high-speed trains.

Now, there are three fundamental significances applied to the transition model in the application. The first is the usage of low-Reynolds number turbulence approaches. The capability of low-Re turbulence approaches to predict transition seems coincidental. Moreover, that's because the calibration of the damping functions is according to reproducing the viscous sublayer specification, not on predicting transition from laminar to turbulent flow. It's accepted which the usage of turbulence approaches without any connection to an intermittency relation emerges to be an irresponsible way of predicting transition. Moreover, low-Re turbulence approaches can be used to bypass transition and are not appropriate for aerodynamic flows [22].

The second method is the so-called e^N approach. It's according to the local, linear stability theory and the parallel flow presumption to estimate the increase of the disturbance domain from the boundary layer neutral point to the transition location. Once the disturbance domain ratio (e^N) exceeds the limiting N factor, transition is supposed to start. The limiting N factor is not known in the improvement and must be decided by calibration to wind tunnel; therefore, the e^N approach is considered a semi-empirical approach. For isolated airfoils, the e^N method has been illustrated to vintage correct transition predictions compared to wind tunnel mensuration. Although, there are some powerful obstacles towards using the e^N approach to general aerospace uses. The first is that since the e^N method is according to linear stability theory, it cannot predict transition due to non-linear influences such as high freestream turbulence or surface roughness. Moreover, common industrial Navier-Stokes solves aren't careful enough to investigate the stability relations. Then, the Navier-Stokes solution must be connected to a detailed boundary layer code. Eventually, the need to track the increase of the disturbance domain ratio due to the streamline findings in a considerable subject for three-dimensional flows where the streamline direction is not equal with the grid [22].

The third method to predicting the communications always related to the free-stream turbulence intensity and the local pressure gradient to the transition momentum thickness Reynolds number transition which is favored by the gas turbine industry, is the usage of actual communications. A typical example is according to a large number of actual perceptions. Whenever this approach demonstrates precise enough, it shows programming and numerical discussions in Navier-Stokes data. For classical communication-based transition approaches, it is needful to compare the real momentum-thickness Reynolds numbers (Re_θ) to the transition amount from the communication ($Re_{\theta t}$). The hardness is connected to non-local equations that are overstated by modern computational fluid dynamics approaches that are according to unstructured grids and massive parallel execution. Unstructured grids do not quickly supply the infrastructure required to integrate global boundary layer parameters because the grid lines normal to the surface can't be simplify recognized [22].

Ji et al. [23], using a new numerical method, investigated the heat transport effects on a high-speed train and especially on its brake system. They did a three-dimensional simulation using a sliding mesh approach to investigate the ventilation and heating of a wheel brake system.

Also, Rashidi et al. [24] Provide a comprehensive review of the most significant numerical and experimental research conducted on high-speed trains in recent years.

The primary purpose of the present numerical investigation is to simulate the time-averaged air-flow around the simplified train model. Four different yaw angles and two different types of surfaces as rough and smooth are considered. The numerical method- $\gamma - \widetilde{Re}_{\theta t}$ transitional model is used to solve the flow field. Different turbulent parameters such as turbulent kinetic energy and dissipation rate are depicted graphically. The aerodynamic forces of pressure coefficient and skin friction coefficient are presented at different cross-sections along the body of the train model comprehensively. There are some novelties in this work, which can be mentioned as 1) Using $\gamma - \widetilde{Re}_{\theta t}$ transitional. Some limited works are utilizing this turbulence model in the analysis of air-flow around high-speed trains. It should be noted that using this model is very useful in the problems to include laminar, laminar/turbulence transition, and fully turbulence regimes. 2) The influence of different yaw angles of crosswind on the local and total aerodynamic coefficient is not negligible. One of the main governing parameters, is analyzed in the present work, is the effect of crosswind yaw angle. 3)

In the real condition, the surface of the considered geometry is not smooth. In this context, in the present investigation, the rough surface is applied to the geometry of the supposed high-speed train. It should be noted that both smooth and rough walls are studied, and the results are compared.

2. Numerical method-$\gamma - \widetilde{Re}_{\theta t}$ transitional model

The main aim of extending the Gamma-Re ($\gamma - Re$) transition approach was to extend a transition approach according to local parameters that could be quickly implemented into current CFD data with unstructured grids and massive parallel execution. The maximum of earlier transition approaches, such as the e^N approach requires to know the structure of the boundary layer and the integration due to that; both meanings are challenging to implement in three dimensions due to various subdivisions of a grid. Another significant insight into the equation of this approach is that the Reynolds vorticity number can be connected to the Reynolds transition onset number. Hence there is a local way to estimate the transition location.

The Gamma-Re transition approach has two relations and is according to the two-equation turbulence approaches in the background of turbulence modeling. This method, both global and local tendencies, can be modeled. The periodic or gamma estimates the percent of the time the flow is turbulent (0 and 1 for fully laminar and fully turbulent, respectively). The periodic works on the production term of the turbulent kinetic energy transport relation in the SST approach to simulate laminarly and turbulence flows. It is worth mentioning, Gamma-Re transition approach is a two-equation approach applied in CFD to improve turbulent transport relations to simulate laminar, laminar-to-turbulent, and turbulence states in a fluid flow. It is beneficial to use this turbulence approach in the problems contained in both laminar and turbulent structures.

This turbulence model consists of two sets of transport equations, which are as follows:

- Intermittency function (γ):

$$\frac{D\gamma}{Dt} = P_\gamma - E_\gamma + \frac{\partial}{\partial x_j}\left[\left(\nu + \frac{\nu_T}{\sigma_f}\right)\frac{\partial \gamma}{\partial x_j}\right], \tag{2.1}$$

Where, the intermittency source terms are defined as:

$$P_\gamma = F_{length} c_{a1} S (\gamma F_{onset})^{0.5} (1 - c_{e1}\gamma); \qquad E_\gamma = c_{a2} \Omega F_{turb} (c_{e2}\gamma - 1). \tag{2.2}$$

The coefficients applied to tune the intermittency equations are:

$$c_{a1} = 2.0; \quad c_{e1} = 1.0; \quad c_{a2} = 0.06; \quad c_{e2} = 50.0; \quad \sigma_f = 1.0.$$

- Transition-onset momentum thickness Reynolds number ($\widetilde{Re}_{\theta t}$):

$$\frac{D\widetilde{Re}_{\theta t}}{Dt} = P_{\theta t} - \frac{\partial}{\partial x_j}\left[\sigma_{\theta t}(\nu + \nu_T)\frac{\partial \widetilde{Re}_{\theta t}}{\partial x_j}\right], \tag{2.3}$$

Where, the intermittency source terms are defined as:

$$P_{\theta t} = c_{\theta t}\frac{Re_{\theta t} - \widetilde{Re}_{\theta t}}{t}(1 - F_{\theta t}); \qquad t = \frac{500\nu}{U^2}, \tag{2.4}$$

The details of closure functions and the related constants are discussed in Langtry and Menter [22]. In the present study, some of the fundamental aspects of modeling will be discussed. The function

F_{onset} is a ratio between the vorticity Reynolds number and a critical amount of the momentum thickness Reynolds number $Re_\nu/(2.193Re_{\theta c})$. On the other hand, the function F_{length} controls the transition region length. The necessary correlations to close this turbulence model can be written as follows:

$$Re_{\theta t} = f\left(Tu,\ \lambda_\theta\right); \qquad Re_{\theta c} = f\left(\widetilde{Re}_{\theta t}\right); \qquad F_{length} = f\left(\widetilde{Re}_{\theta t}\right). \tag{2.5}$$

As is mentioned above, a transition onset momentum thickness Reynolds number is denoted by the quantity $Re_{\theta t}$. Its expression as a function of the Thwaites parameter λ_θ and turbulence intensity Tu which, are given in [22]. This kind of variable is estimated at any arbitrary point of the computational domain locally. The function is defined as follows:

$$F_{\theta t} = min\left[max\left(F_{wake}e^{-\left(\frac{y}{\delta}\right)^4},\ 1 - \frac{\gamma - 1/C_{e2}}{1 - 1/C_{e2}}\right),\ 1\right], \tag{2.6}$$

where;

$$F_{wake} = e^{-\left(\frac{Re_\omega}{10^5}\right)^2}; \qquad Re_\omega = \frac{\omega y^2}{\nu}; \qquad \delta = 375\frac{\widetilde{Re}_{\theta t}\nu y \Omega}{U^2}. \tag{2.7}$$

Appearing in the source term of Eq. (2.3). This function is designed to be equal to 1 in the boundary layer and 0 in the freestream to activate the source term $P_{\theta t}$ and force the transported quantity $\widetilde{Re}_{\theta t}$ to have an equal value with the transition onset momentum thickness Reynolds number $Re_{\theta t}$.
Let the prediction of pragmatic reattachment locations in separation-induced transition, a correction for the intermittency factor presented in Eq. (2.8) by defining a "separation aware" proposed by Langtry and Menter [22]

$$\gamma_{sep} = min\left\{2max\left[\frac{Re_\nu}{3.235Re_{\theta c}} - 1,\ 0\right]F_{reattach},\ 2\right\}F_{\theta t}, \tag{2.8}$$

where;

$$F_{reattach} = exp\left[-(Re_T/20)^4\right]. \tag{2.9}$$

And effective intermittency could be defined as follows:

$$\gamma_{eff} = max\left(\gamma,\ \gamma_{sep}\right), \tag{2.10}$$

This function is used by Langtry and Menter [22] in the coupling with the turbulence approach. Moreover, the role of two new equations must be declared. The Eqs. (2.9) and (2.10) allow the effective intermittency to be increased above 1 in the regions of transitional separated flow.
To prevent the function $F_{\theta t}$ changes to be equal to 1 outside of the boundary layer and the parameter δ to become very large in the unsteady calculations, the parameter δ can be defined as follow:

$$\delta = 170\frac{\widetilde{Re}_{\theta t}\nu}{U}, \tag{2.11}$$

However, it should be noted that such a modification has a minor influence on the predictions in the steady transitional problems.
The logarithmic law at the adjacent of the rough wall can be defined as follows:

$$\frac{u}{u^*} = 2.5ln\frac{z}{k_s} + 8.5 = 2.5ln\frac{z}{z_0}, \tag{2.12}$$

where u^* represents the friction velocity, z represents the distance to that wall, and k_s is the equivalent roughness. Also, the value of z for $u = 0$ can be considered as the value of $z_0 = k_s/30$. Also, the value of z_0 will be defined by the following expression for the smooth wall:

$$z_0 = 0.113\frac{\nu}{u^*}, \tag{2.13}$$

Where ν is the kinematic viscosity of operating fluid (air). The Eq. (2.13) may be modified by using z_0:

$$u/u^* = 2.5ln\left(u^* z/\nu\right) + 5.45. \tag{2.14}$$

Which is the classical explanation of the logarithmic region of the law of the wall for a smooth surface.

3. Geometry and boundary conditions

As it was mentioned before, there are some logical reasons to use a simplified small-scale model instead of a real high-speed train with full-scale. Furthermore, in all researches, the numerical simulation is critical to be performed besides the experimental investigations. Some of the reasons are 1) Limited wind tunnel equipment, 2) Limited data in experimental investigations, 3) Limited computer resources, and 4) Limited experimental and numerical resources to cover all complex details. Also, it is worth mentioning that Baker et al. [6] carried out some experiments on the full-scale train at a coastal site. The main purpose of these experimental works was to identify the characteristics of flow around a full-scale train and measure the time-averaged and instantaneous coefficients. They concluded that the obtained results from a small-scale model (1/30 scale model) in the wind tunnel with the results of the full-scale model are in close agreement. Also, there are some deviations in the vertical component of aerodynamic forces, such as lift force caused by the local roughness variations in the proximity to the wind tunnel models affecting underbody flow. It can be concluded that the results of a wind tunnel test are reliable enough to use in engineering design or numerical validation. In the present study, the simplified model of a high-speed train used by Chiu and Squire [12] investigates the effect of nose shape on the flow structure. The equation related to the cross-sectional profile of the simplified train model is as follows:

$$|y|^n + |z|^n = c^n, \tag{3.1}$$

Where the value of constant and power are as follow:

$$c = D/2 = 62.5\ mm, \qquad n = 5. \tag{3.2}$$

The schematic of the considered geometry is resented in Fig. 1. The train body has a cylindrical form with a height, and length of $D = 125\ mm$ and $9.36D$, respectively. It should be noted that the cross-section profile, height, and length of all cases are identical. The nose cross-section is assumed by the same relation, where $c$follows a semielliptical shape with a primary diameter of $1.28D$ and $0.64D$ for the long-nose and the short-nose approaches, respectively. At the same time, n decreases uniformly to 2 at the nose tip. To simulate the experimental setup, it is worth to pay attention to all details. In this context, the train is located on a channel like the wind tunnel, as shown in Fig. 1. The authors attempted to consider all scales and boundary conditions like the real one as well. The channel has a length of $29D$ in the direction of streamwise, a height of $9.76D$, and a width of $13.4D$

perpendicular to streamwise. The train model is mounted at the channel (wind tunnel) horizontally. Moreover, the distance of the bottom side of the model to the ground is considered to be $0.15D$ as a real high-speed train. The centerline of the model is considered to be $8D$ from the inlet and $21D$ from the outlet of the channel due to capturing all downstream events. In the experimental setup, a ground-board was used above the tunnel floor to control the boundary layer increase. Also, four adjustable flaps were mounted at the end of the rear the ground-board to control the flow so that the mainstream was parallel to the ground-board when approaching its leading edge. To simulating the ground-board boundary condition at the numerical study, the bottom of the computational domain is placed at the height of the ground-board.
The boundary conditions of the inlet, outlet, surrounding walls, and surface of train body are as follows:

1. Inlet: entering flow with uniform velocity with a constant profile of V_{Wind}
2. Front: entering flow with uniform velocity with a constant profile of V_{Train}
3. Outlet: convective boundary condition, $\partial\overline{u}_i/\partial t + U_\infty\left(\partial\overline{u}_i/\partial z\right) = 0$, where U_∞ is the freestream velocity magnitude
4. Back: convective boundary condition, $\partial\overline{u}_i/\partial t + U_\infty\left(\partial\overline{u}_i/\partial z\right) = 0$, where U_∞ is the freestream velocity magnitude
5. Up: convective boundary condition, $\partial\overline{u}_i/\partial t + U_\infty\left(\partial\overline{u}_i/\partial z\right) = 0$, where U_∞ is the freestream velocity magnitude
6. Surface of train body: no-slip boundary condition is used
7. Channel floor: no-slip boundary condition with is used and $V = 0$

It must be noted that the Neumann boundary condition for the pressure is used for all boundaries. Four different directions for the velocity in different yaw angles ($\theta = 10°,\ 20°,\ 30°,\ and\ 40°$) are considered, which is defined as $\theta = tan^{-1}\left(\frac{V_{Wind}}{V_{Train}}\right)$.
The ground is usually assumed as rough, whenever two conditions, rough and smooth, are presented for the train surface. The underbody of the train includes some ancillary sets, so that it can be assumed as a rough surface with large values of roughness. To reduction the simulation, the train surface is assumed in its case as a uniform rough surface. Moreover, to that, it is considered that the ground to have a uniformly roughness. In this context, z_0 is 2 mm and 0.03 mm for the ground and the train surface, respectively.

4. Numerical accuracy

The geometry of the simplified train model is constructed by the equation mentioned above (3.1). To improve the mesh quality, another dummy train (refine box) with a higher dimension is created around the original geometry. The height of the dummy train is equal to $1.15D$, and the hexahedral mesh form is employed in this region around the actual train. Also, an O-type mesh is applied between the created gap of innovative and dummy models in the belt of the thickness of $0.075D$. As a result of this method, the smooth mesh can be made. The present work is carried out with a high-performance computer system, predicting the three-dimensional flow structure around the simplified train with high grid numbers. The SST transitional equations are discretized with the three-dimensional finite volume approach. The viscous convective diffusion is approximated using a second-order central difference plan. Furthermore, the upwind method is not used to decrease the numerical dissipation. The central difference scheme is sensitive to the stretching ratio in the region with large flow variations. It is necessary to keep the mesh stretching ratio below 1.1 in the O-type

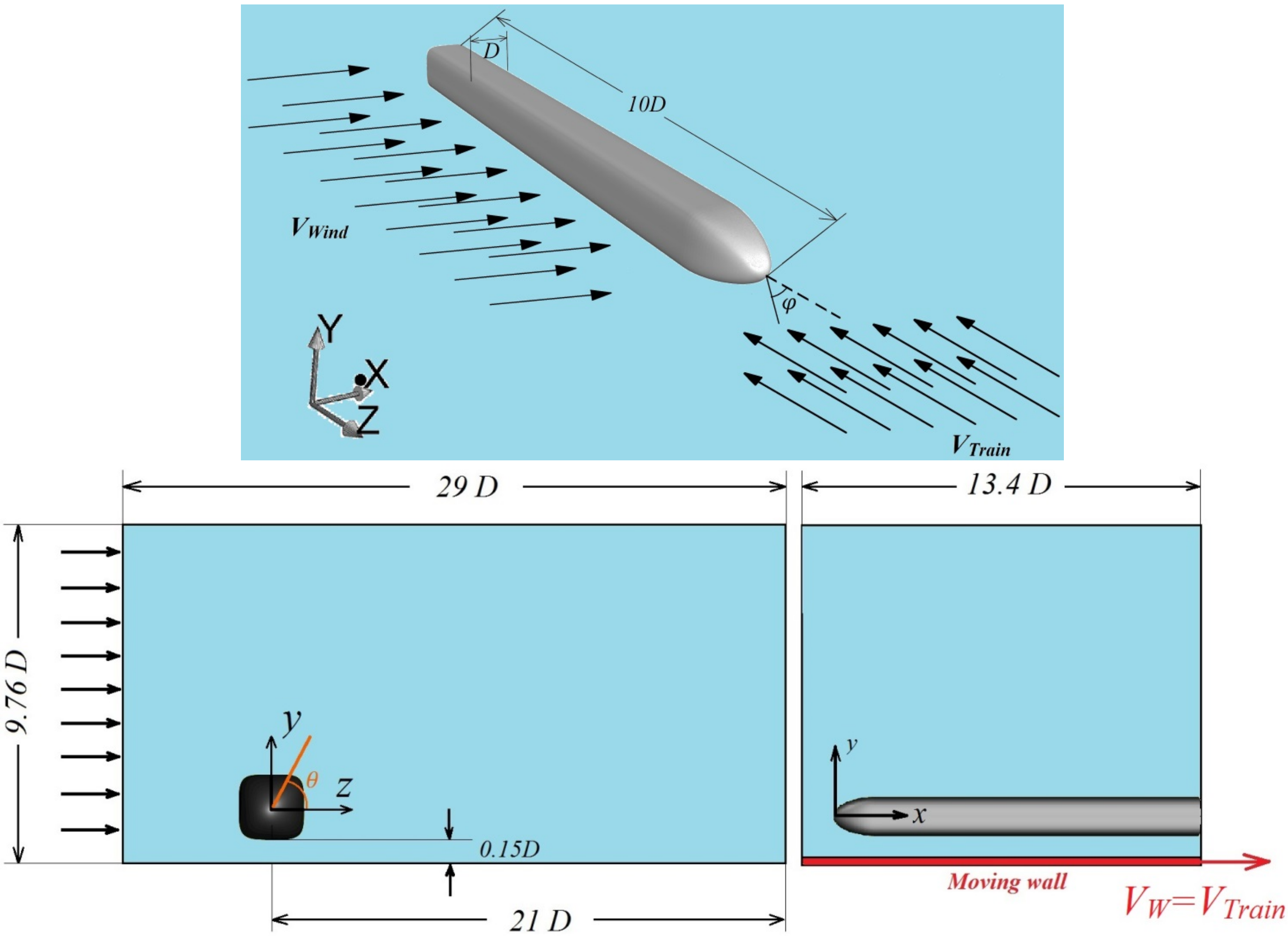

Figure 1: Details of studied geometry and computational domain.

meshes at the adjacent of the original model where the large flow changes are expected. To couple the pressure terms to the velocity terms, the SIMPLE algorithm is employed.

The distributions of time-averaged pressure at different sections of the simplified train model are compared with the experimental results of the similar models, and related physical boundary conditions are presented in Fig. 1. The local pressure coefficient (C_P) is utilized to express time-averaged pressure distribution. The pressure coefficient (C_P) is defined as follows:

$$C_P = \frac{\langle P \rangle_t - P_\infty}{\frac{1}{2}\rho U_\infty^2} \tag{4.1}$$

Here U_∞ is the air-flow velocity as the freestream, P_∞ is the reference pressure. The amount of the reference pressure is chosen from the top corner of the inlet channel since the distance is sufficient to avoid the possible influence of the model on the total inlet pressure.

5. Results and discussion

In the present study, the three-dimensional turbulent flow around a simplified train model with a constant magnitude of freestream velocity at four different yaw angles (four different yaw angles) with the SST transitional turbulence model ($\gamma - \widetilde{Re}_{\theta t}$) is carried out. The three-dimensional flow structure, two-dimensional streamlines at various sections along the length of simplified train model for presenting details, turbulence quantities such as turbulence kinetic energy and turbulent dissipation rate, pressure and pressure coefficient, and skin friction coefficient are presented graphically and quantitative which render comprehensive insight about the influences of the yaw angle around a high-speed train. It can be observed in Figs. 2 and 3 that a comparison between the present simulations and the experimental findings performed by Chiu [13] that there are fair agreements between the numerical and experimental. As such, it can be verified that the present numerical simulations predict the three-dimensional flow structure, turbulence quantities, and other local and total parameters accurately.

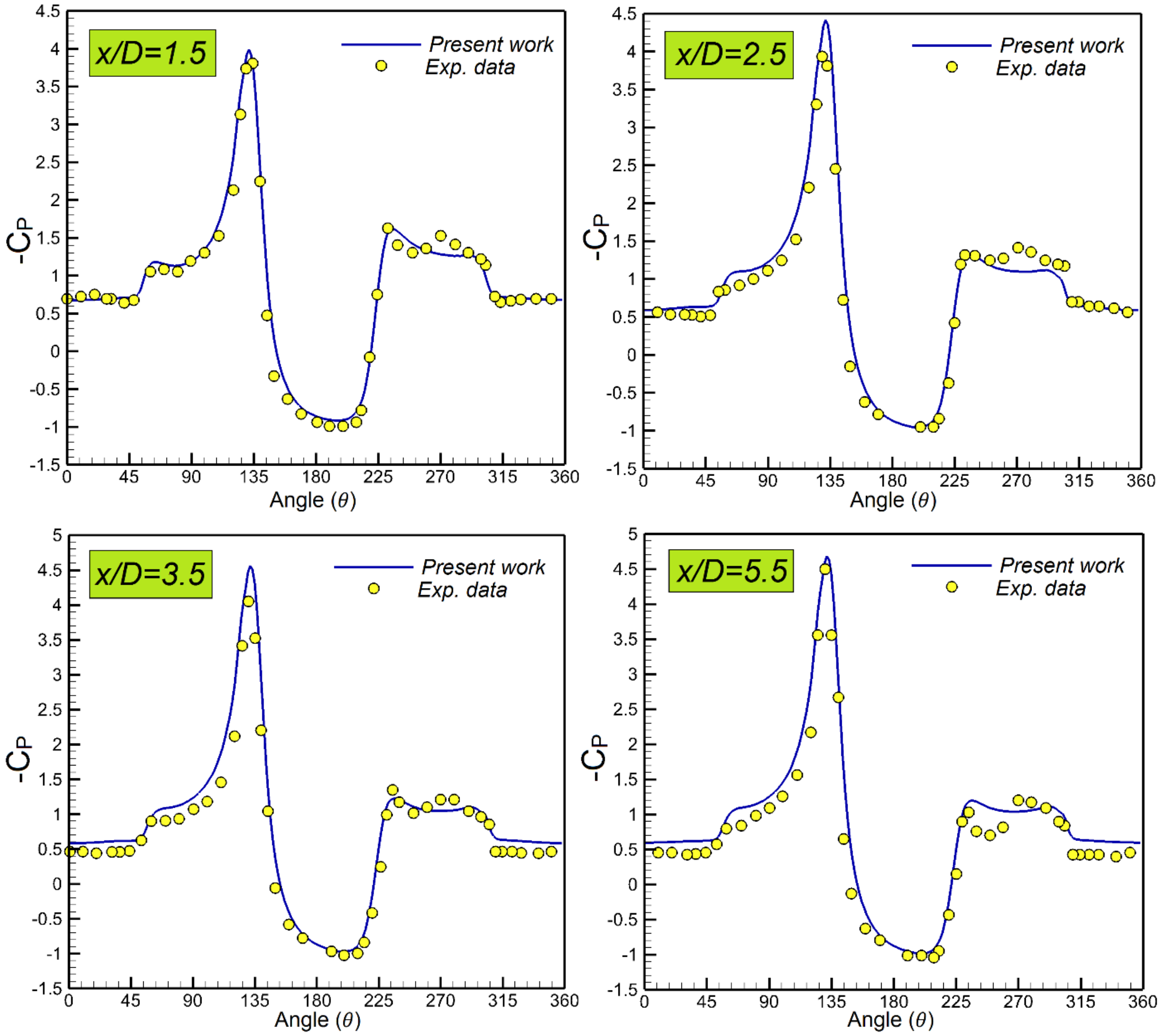

Figure 2: Comparison between results of the present work at $\theta = 0°$ and experimental results performed by Chiu [13].

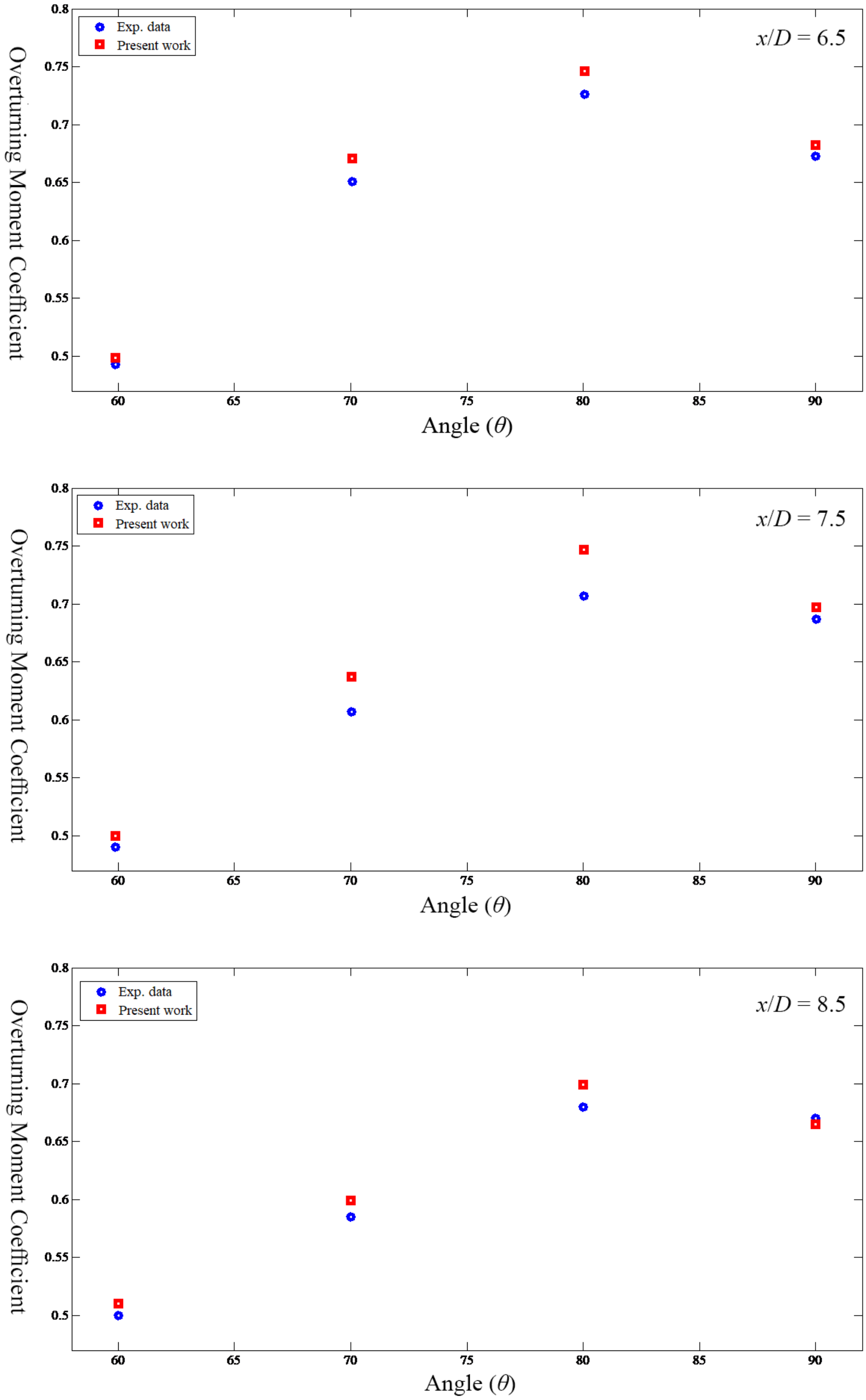

Figure 3: Comparison between results of the present work for x/D = 6.5, 7.5 and 8.5., and experimental results performed by Chiu [13].

5.1. Three-dimensional flow structure analysis

The flow structure behind the train is significantly influenced by the yaw angle. Different three-dimensional flow structure around the train at four different yaw angles ($\theta = 10°,\ 20°,\ 30°,$ and $40°$) perpendicular to the y-axis are presented in Fig. 4. It should be noted that the velocity magnitude of front wind is constant, and the velocity magnitude of crosswind is variable as the yaw angle changes. As shown in Fig. 4, the circulations at the lee-side of the simplified train model are created. These circulations at each section along the length of the model are consist of two main circulations, which are kindled from the roof-side and bottom-side of the model. Moreover, the height and width of the circulation changes along the height of the model. Furthermore, the nose of the simplified train model causes reducing the helical flow. The flow travels along the surface of the nose omitting the three-dimensional spiral flow structure. It should be noted that the circulation existing at the Lee-ward of the model increases the pressure coefficient and resulted in drag force. As such, it is necessary to identify the nature of the circulations and finding the methods to omit them. The created vortices at the adjacent of the nose of the model are pulled inside of the main circulation, which is caused by both the curvy shape of the nose and negative pressure of main circulations. In the cases with a lower yaw angle, the spiral flow travels at the adjacent of the simplified train body. On the contrary, the flow separates from the body in a higher wind angle as the flow imposes to the train's side.

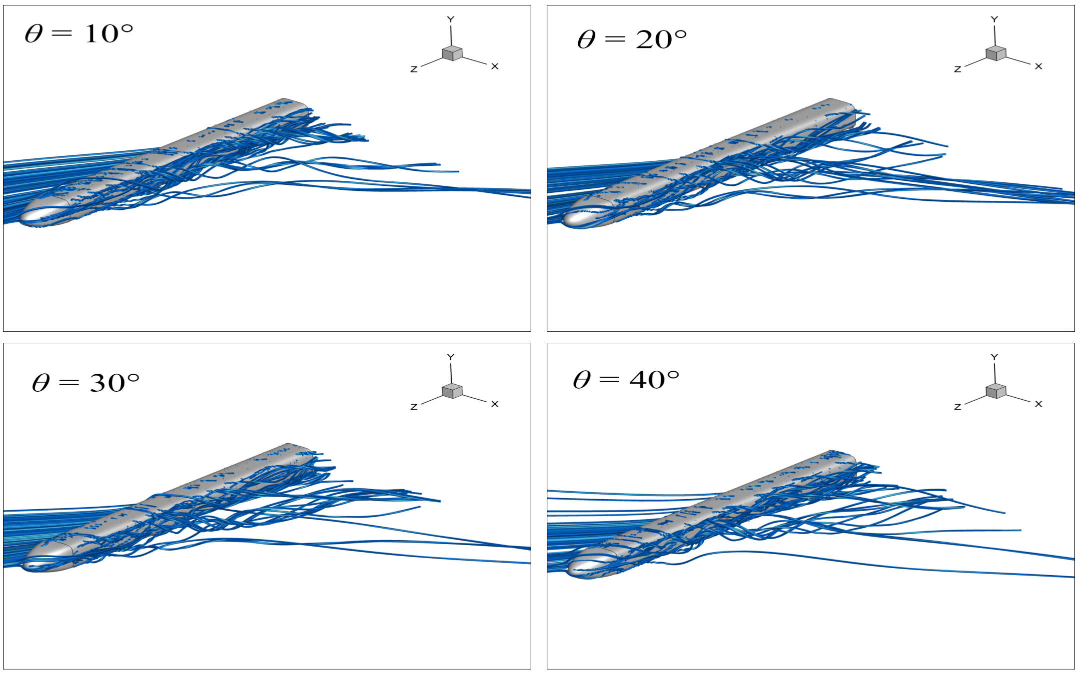

Figure 4: Three-dimensional time-averaged flow structures for different yaw angles.

5.2. Two-dimensional streamlines analysis

For a better understanding of the flow pattern around the simplified high-speed train, the three-dimensional flow structures are visualized at different sections along the length of the train model and perpendicular to the x-axis. The two-dimensional streamlines are depicted graphically, shown in Fig. 5, at six different sections as $x/D = 1.5,\ 2.5,\ 3.5,\ 4.5,\ 6.5,$ and 8.5 for four different yaw angles

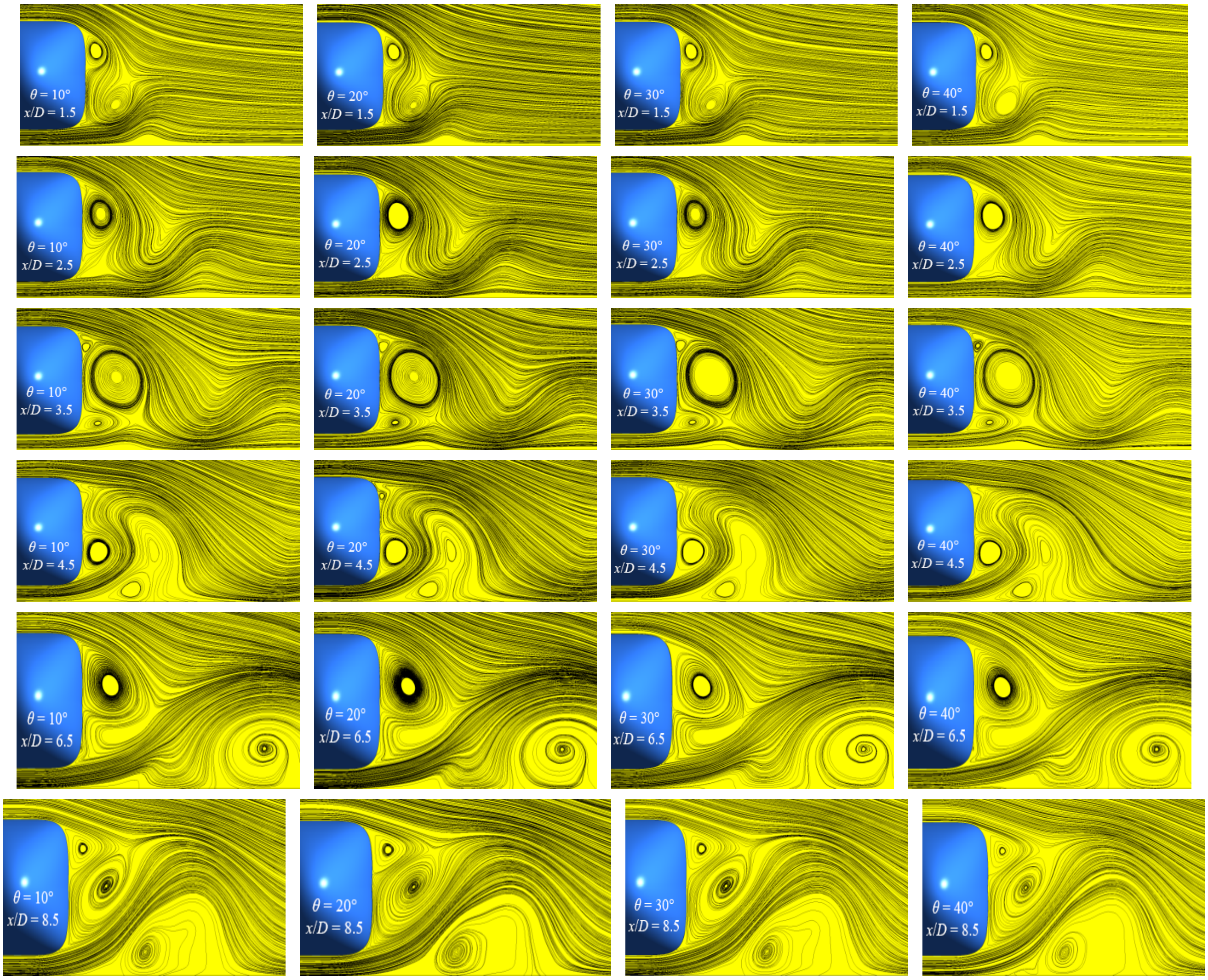

Figure 5: Time-averaged streamlines at different cross-sections along the train model body at various yaw angles for rough train body.

of $\theta = 10°,\ 20°,\ 30°,$ and $40°$. It can be observed that the velocity magnitude at the top of the model is high, especially at the left-top corner of the model, since the streamlines are compacted at these regions. Also, the strong streamlines exist at the gap between train and ground. Since this confined gap acts like a nozzle enhancing the velocity magnitude and reducing the pressure. At $x/D = 1.5$, which is near to the nose of the model, there are two small circulations, which show that the spiral flow starts to being created and creating reverse flow as well. Also, the flow pattern in the cases with $\theta = 10°$ and $\theta = 20°$, $\theta = 30°$, and $\theta = 40°$ are almost similar to each other. In case $x/D = 2.5$, the circulations become more significant the spiral flows grow.

5.3. Surface streamlines at wind-ward

To a comprehensive investigation of the flow structure, the flow pattern at the two most important regions of wind-ward and Lee-ward is analyzed. The Lee-ward flow patterns are identified by three-dimensional and two-dimensional flow patterns. The three-dimensional flow structures at the wind-ward will not render clear insight; the streamlines at the surface of the simplified train model are obtained in Fig. 6. It can be observed that the positions of the stagnation lines at the surface of the

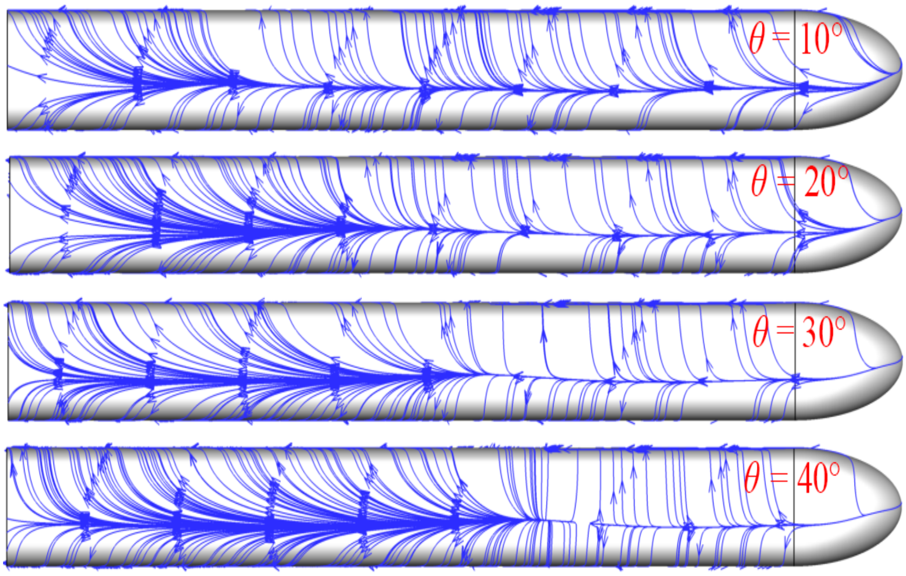

Figure 6: Surface streamlines at the wind-ward wall for various yaw angles for rough train body.

model's body are almost similar for all cases. On the other hand, the stagnation lines at the model's nose are deflected to the roof of the model. The air-flow is imposed to be passed from the top due to limited space at the bottom of the train model.

5.4. Turbulent Kinetic energy

As the air stream collides with the simplified train model, the regime of the air-flow stream changes forms laminar to turbulent. The zones with the turbulent regime and the intensity of turbulence may be identified with the turbulent kinetic energy parameter. The time-averaged turbulent kinetic energy parameter iso-surfaces for four different yaw angles are depicted graphically in Fig. 7. The iso-surfaces of turbulent kinetic energy are obtained at various levels with transparency to better detect regions with different turbulence intensity. It should be noted that the iso-surface diagrams of each case must be considered with theirs related turbulent kinetic energy ranges next to each case, not just by color. In the case of $\theta = 0°$, the contour of turbulent kinetic energy is more pronounced at the back sections of the train. Since the flow travels along the train body smoothly because of the curvy nose of the train. As the yaw angle increases, the contour of turbulent kinetic energy grows and covers the train body since the fluid flow becomes turbulent as the crosswind collides with the body. Furthermore, the contour of turbulent kinetic energy increases as the surface of the train body becomes rough. The flow colliding to the rough surface will have more turbulent nature concerning a smooth surface.

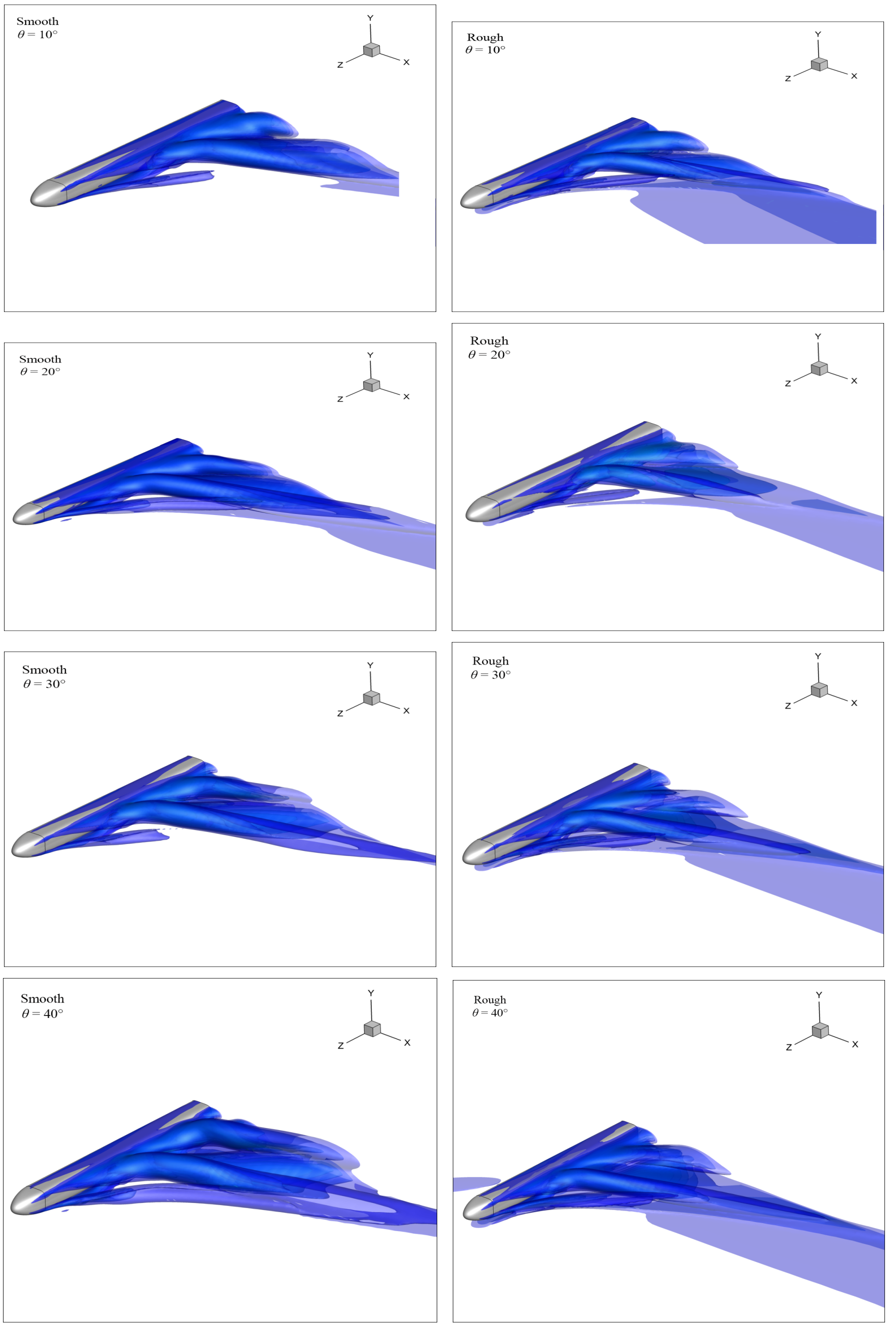

Figure 7: Iso-surfaces of turbulent kinetic energy for different yaw angles.

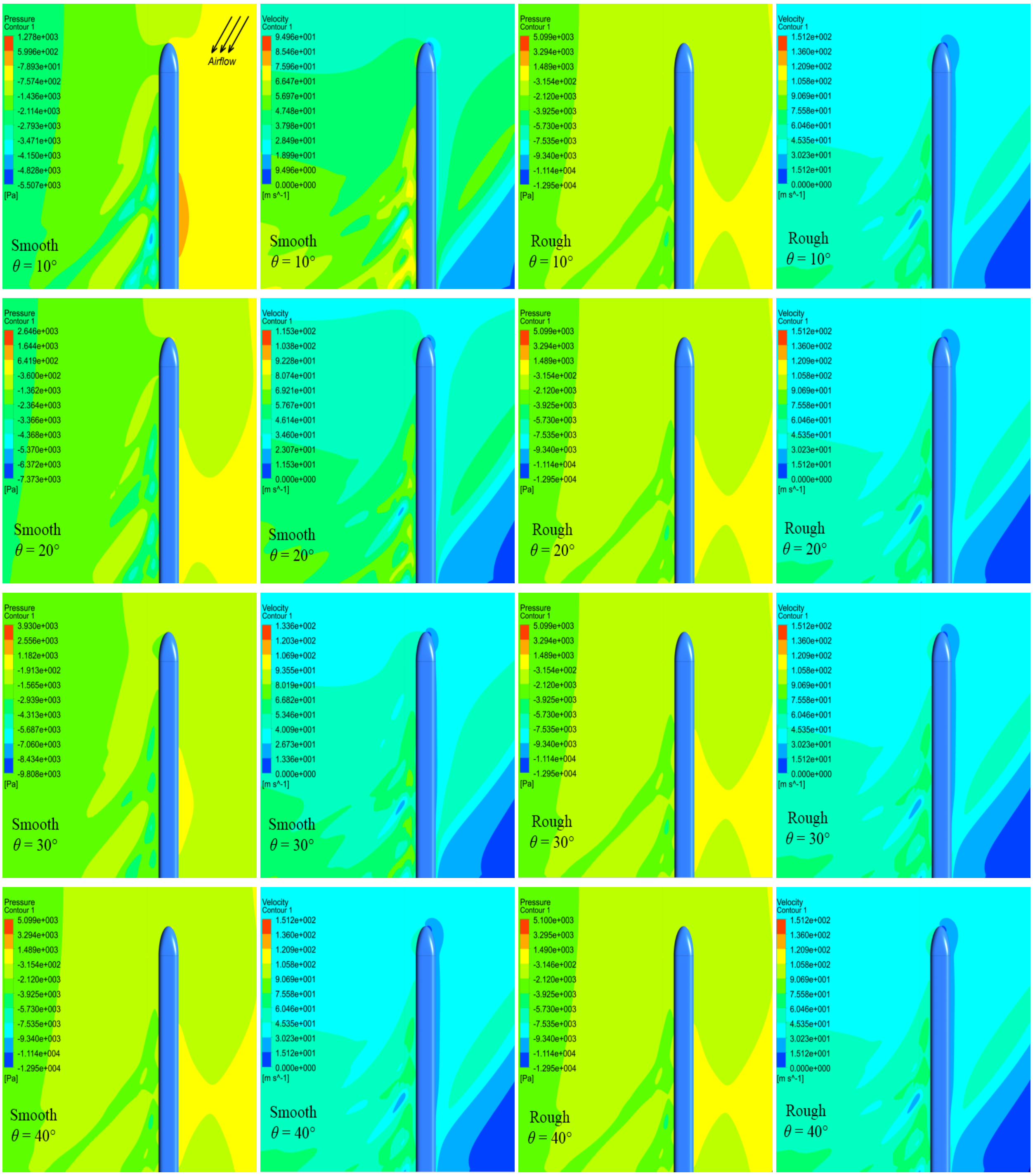

Figure 8: Velocity and pressure fields for different yaw angles and surface types.

5.5. *Velocity and pressure field*

The pressure and velocity fields at a section on the surface of the z-axis and perpendicular to the y-axis for different yaw angles, smooth and rough surfaces are presented in Fig. 8. It can be observed that the pressure and velocity fields are various at different yaw angles and type of surface. As the yaw angle increases, the magnitude of pressure behind the train decreases. This matter occurs at both smooth and rough train bodies. It should be noted that the magnitude of total pressure around the train has no considerable difference in different cases, the pressure distribution has a concise difference in different yaw angles and types of surfaces. Similarly, this matter occurs for the velocity field.

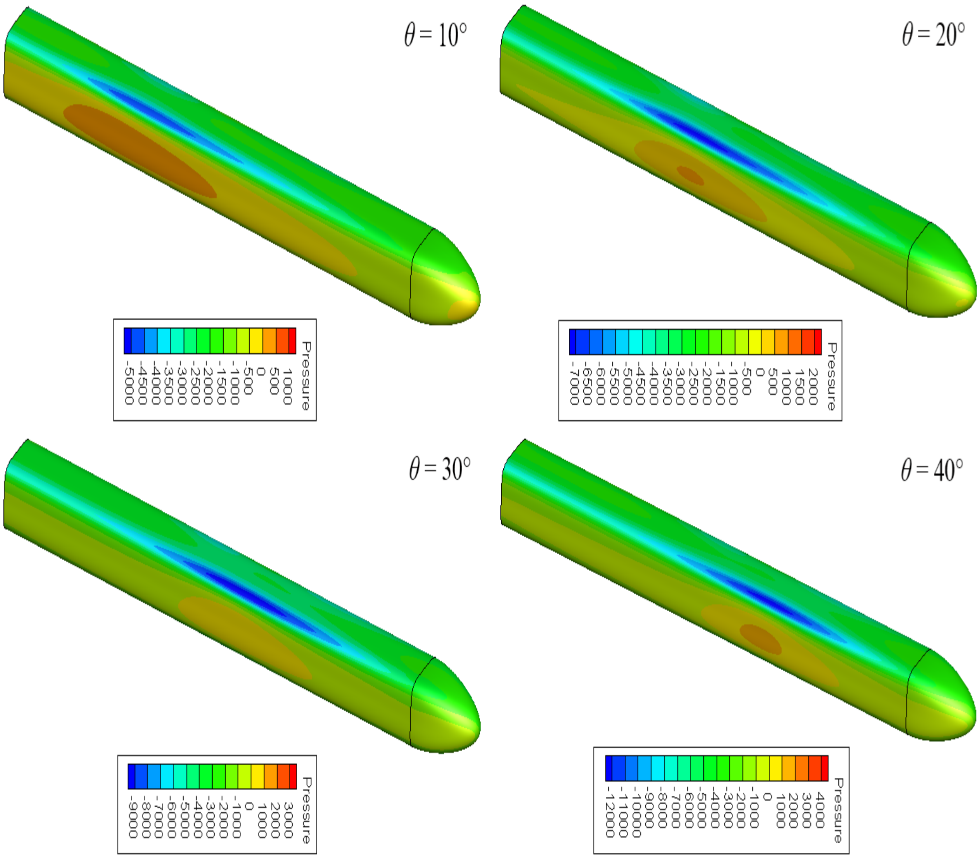

Figure 9: Contours of total pressure for different yaw angle angles.

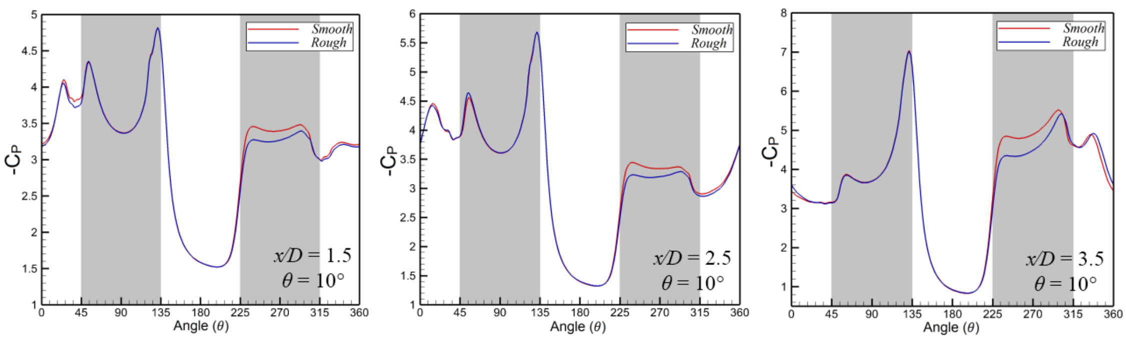

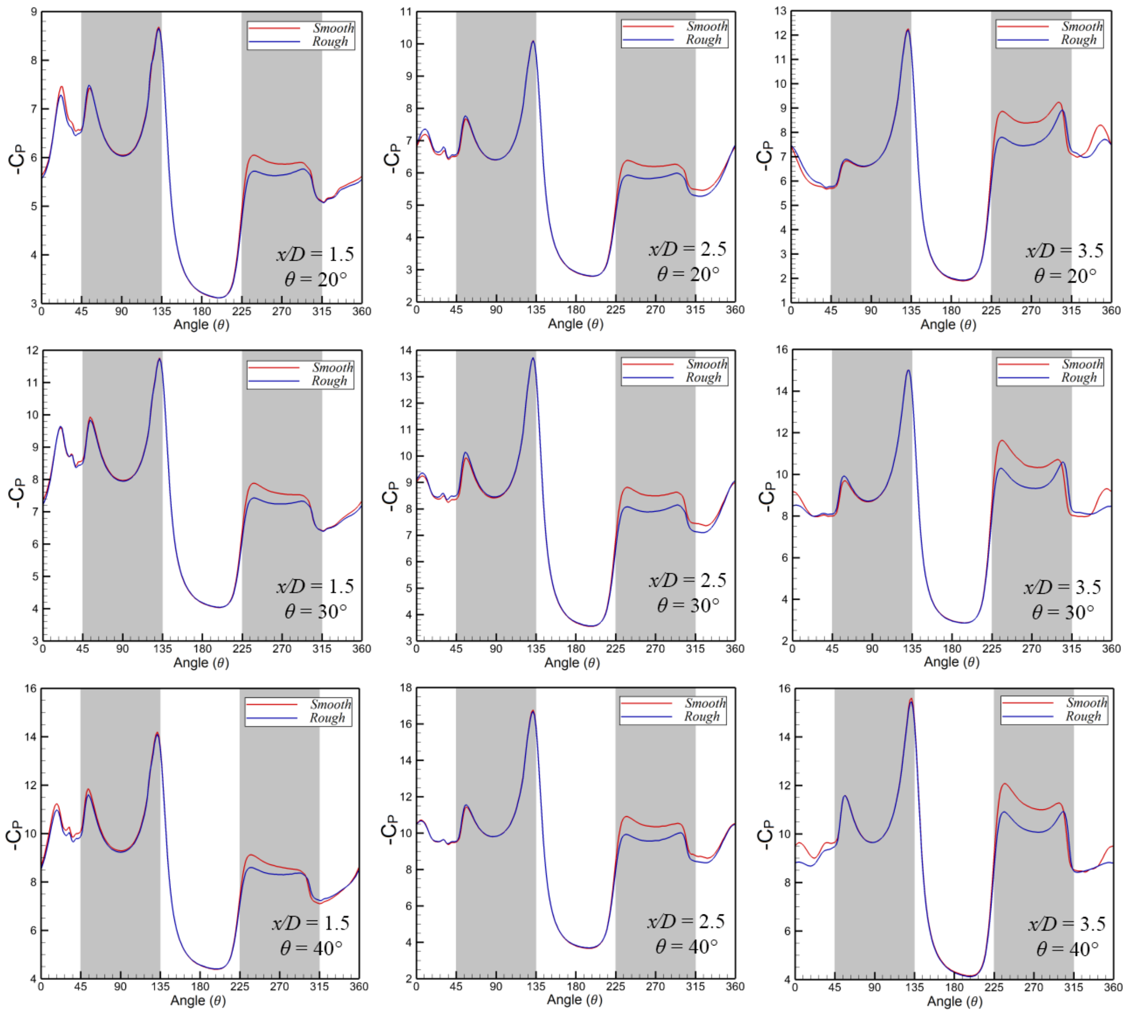

Figure 10: Values of pressure coefficient for two various yaw angles ($\theta = 10°,\ 20°,\ 30°,$ and $40°$) at different cross-section along the train model body.

5.6. *Total pressure*

The total pressure contours for different yaw angles ($\theta = 10°,\ 20°,\ 30°,$ and $40°$) are presented in Fig. 9. It can be observed that the contours of the total pressure on the surface of the simplified train model are almost similar to each other. The wind-ward wall of the model's body is affected by the most proportion of the total pressure. Furthermore, the curvy form of the nose causes that the maximum value of pressure is stopped to occur on the nose. In this context, it is clear that the train's nose sustains the lower value of the total pressure concerning the same area at the model's body. In all cases, the top edge of the wind-ward model has low pressure due to air-flow jumping at this region and creating a low-pressure zone.

5.7. *Pressure coefficient*

he pressure coefficients on the surface of the simplified train model for different yaw angles ($\theta = 10°,\ 20°,\ 30°,$ and $40°$) to varying cross-sections along the length (x-axis) of the model ($x/D = 1.5,\ 2.5,$ and 3.5) for the rough train body are presented in Fig. 10. It is worth to mention that all discussions in this section are based on the negative value of the pressure coefficient, and each part of the body of the simplified train model belongs to a specific range of rotation angle on the surface of the model as follows:

1. Lee-ward: $315° < \theta < 360°$ and $0° < \theta < 45°$
2. Roof: $45° < \theta < 135°$
3. Wind-ward: $135° < \theta < 225°$
4. Bottom: $225° < \theta < 315°$

As shown in this figure, the trends of increasing and reducing the pressure coefficient for all cases at each cross-section are almost similar to each other. At the roof of the model, the negative value of the pressure coefficient increases with increasing rotation angle (θ), and the pressure coefficient is maximum at the top edge at the wind-ward direction ($\theta = 135°$). At the wind-ward wall at the rotation angle range of $135° < \theta < 225°$, the lowest value of the native pressure coefficient occurs. Since the air-flow collides with the simplified train model directly. In this range, the negative value of the pressure coefficient decreases and then increases. In the next part of the train model in the rotation angle range of $225° < \theta < 315°$ (Bottom), there are no considerable differences in the pressure coefficient. Since the bottom of the train model does not affect by the freestream directly, and the flow jumping does not occur due to limited space at the bottom of the model.

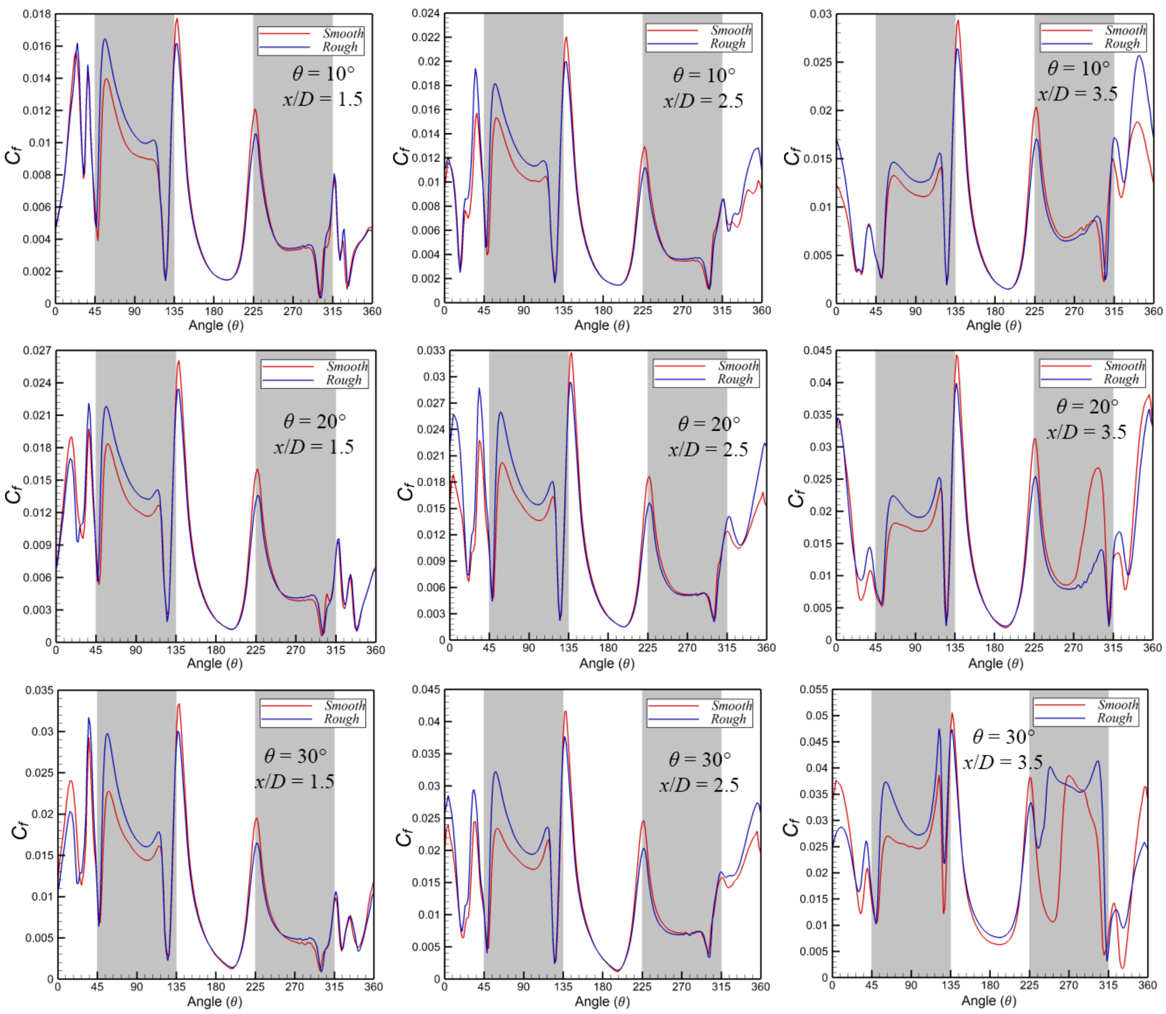

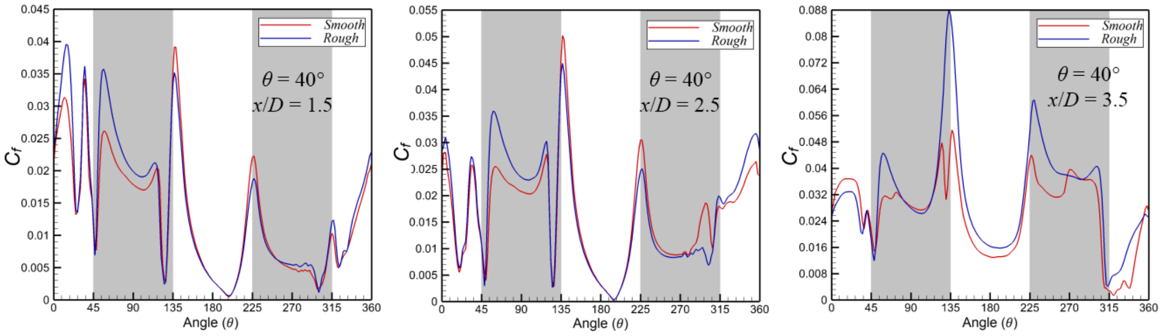

Figure 11: Values of skin friction coefficient for two different yaw angles ($\theta = 10°,\ 20°,\ 30°,$ and $40°$) at different cross-section along the train model body.

5.8. Skin friction coefficient

The pressure coefficients on the surface of the simplified train model for different yaw angles ($\theta = 10°, 20°, 30°,$ and $40°$) to varying cross-sections along the length (x-axis) of the model ($x/D = 1.5,\ 2.5,\ 3.5,$ and 5.5) are presented in Fig. 11. It should be noted that the range of rotation angle for the train model is as same as the previous section. The mainstream of the changing of the skin friction coefficient for all cases is almost similar to each other. It can be observed that the skin friction coefficient has a lower value at the surface of the bottom wall, virtually in all cases. On the other hand, the maximum value of the skin friction coefficient occurs at the top edge of the wind-ward wall. Moreover, in comparison to smooth and rough train bodies, skin friction has slight differences in some regions.

6. CONCLUSIONS

The main objective of the present numerical investigation is to analyze the air-flow over the simplified high-speed train. The $\gamma - \widetilde{Re}_{\theta t}$ transitional model is applied to predict the time-averaged three-dimensional flow structure, turbulence quantities and the aerodynamic forces at four different yaw angles of $\theta = 10°,\ 20°,\ 30°,$ and $40°$ and two different types of smooth and rough train surfaces. The following results can be listed:

1. The flow direction angle has a pronounced influence on the three-dimensional flow structure around the model.
2. The pressure coefficient and skin friction coefficient increase with the increasing yaw angle.
3. The curvy nose of the simplified train model has considerable influences on determining the vortex and its turbulent nature at the lee-ward region.
4. The distributions of the skin friction and pressure coefficients are affected by the yaw angle.
5. The Influence of roughness on the pressure coefficient is negligible.
6. The Influence of roughness on skin's friction coefficient is local. In some regions, the skin friction coefficient increases in rough train surfaces.

References

[1] C. Catanzaro, F. Cheli, D. Rocchi, P. Schito and G. Tomasini, *High-speed train crosswind analysis: CFD study and validation with wind-tunnel tests*, Int. Conf. Engin. Conf. Int. Aerodyn. Heavy Vehicles III. (2016) 99–112.

[2] H. Hemida and S. Krajnović, *LES study of the influence of the nose shape and yaw angles on flow structures around trains*, J. Wind Engin. Indust. Aerodyn. 98(1) (2010) 34–46.

[3] C.J. Bakera, J. Jones, F. Lopez-Calleja and J. Mundayd, *Measurements of the cross wind forces on trains*, J. Wind Engin. Indust. Aerodyn. 92(7) (2004) 547–563.

[4] M.M. Fragner, K.A. Weinman, R. Deiterding, U. Fey and C. Wagner, *Comparison of industrial and scientific CFD approaches for predicting cross wind stability of the NGT2 model train geometry*, Int. J. Railway Tech. 4(1) (2015) 1–28.

[5] J. García, A. Crespo, A. Berasarte and J. Goikoetxea, Study of the flow between the train underbody and the ballast track, J. Wind Engin. Indust. Aerodyn. 99(10) (2011) 1089–1098.

[6] C. Baker, The simulation on of unsteady aerodynamic cross wind forces on trains. J. Wind Engin. Indust. Aerodyn. 98.2 (2010) 88–99.

[7] S. Diasinos, T.J. Barber and G. Doig, *The effects of simplifications on isolated wheel aerodynamics*, J. Wind Engin. Indust. Aerodyn. 146 (2015) 90–101.

[8] C. Paz, E. Suárez, C. Gil and M. Concheiro, *Numerical study of the impact of windblown sand particles on a high-speed train*, J. Wind Engin. Indust. Aerodyn. 145 (2015) 87–93.

[9] T. Li, M. Yu, J. Zhang and W. Zhang, *A fast equilibrium state approach to determine interaction between stochastic crosswinds and high-speed trains*, J. Wind Engin. Indust. Aerodyn. 143 (2015) 91–104.

[10] C. Xia, X. Shan and Z. Yang, *Wall interference effect on the aerodynamics of a high-speed train*, Procedia Engin. 126 (2015) 527–531.

[11] J. Copley, *The three-dimensional flow around railway trains*, J. Wind Engin. Indust. Aerodyn. 26(1) (1987) 21–52.

[12] T. Chiu and L. Squire, *An experimental study of the flow over a train in a crosswind at large yaw angles up to 90*, J. Wind Engin. Indust. Aerodyn. 45(1) (1992) 47–74.

[13] T. Chiu, *Prediction of the aerodynamic loads on a railway train in a cross-wind at large yaw angles using an integrated two-and three-dimensional source/vortex panel method*, J. Wind Engin. Indust. Aerodyn. 57(1) (1995) 19–39.

[14] U. Hoppmann, S. Koenig, T. Tielkes and G. Matschke, *A short-term strong wind prediction model for railway application: design and verification*, J. Wind Engin. Indust. Aerodyn. 90.10 (2002) 1127–1134.

[15] M. Suzuki, K. Tanemoto and T. Maeda, *Aerodynamic characteristics of train/vehicles under cross winds*, J. Wind Engin. Indust. Aerodyn. 91(1) (2003) 209–218.

[16] B. Diedrichs, *On computational fluid dynamics modelling of crosswind effects for high-speed rolling stock*, Proc. Instit. Mech. Engin. Part F: J. Rail Rapid Trans.217(3) (2003) 203–226.

[17] H. Hemida, S. Krajnovic and L. Davidson, *Large-eddy simulation of the flow around a simplified high speed train under the influence of a cross-wind*, 17th AIAA Comput. Fluid Dyn. Conf. 2005.

[18] W. Khier, M. Breuer and F. Durst, *Flow structure around trains under side wind conditions: a numerical study*, Comput. Fluids 29(2) (2000) 179–195.

[19] J. García, J. Munoz-Paniagua and A. Crespo, *Numerical study of the aerodynamics of a full scale train under turbulent wind conditions, including surface roughness effects*, J. Fluids Struct. 74 (2017) 1–18.

[20] Y. Zhuang and X. Lu, *Numerical investigation on the aerodynamics of a simplified high-speed train under cross-winds*, Theo. Appl. Mech. Lett. 5(5) (2015) 181–186.

[21] C. Baker, *The flow around high speed trains*, J. Wind Engin. Indust. Aerodyn. 98(6) (2010) 277–298.

[22] R.B. Langtry and F.R. Menter, *Correlation-based transition modeling for unstructured parallelized computational fluid dynamics codes*, AIAA J. 47(12) (2009) 2894–2906.

[23] P. Ji, F. Wu, G. Zhang, X. Yin and D. Vainchtein, *A novel numerical approach for investigation of the heat transport in a full 3D brake system of high-speed trains*, Numerical Heat Trans. Part A: Appl. 75(12) (2019) 824–840.

[24] M.M. Rashidi, A. Hajipour, T. Li, Z. Yang and Q. Li, *A review of recent studies on simulations for flow around high-speed trains*, J. Appl. Comput. Mech. 5(2) (2019) 311–333.

Nomenclature

C_P	pressure coefficient
k	turbulent kinetic energy
k_l	laminar kinetic energy
Re	Reynolds number
Re_θ	momentum thickness Reynolds number, $u\theta/\nu$
Re_T	turbulent Reynolds number, $k/(\nu\omega)$
$Re_{\theta t}$	transition onset momentum thickness Reynolds number (transported quantity)
$Re_{\theta c}$	critical momentum thickness Reynolds number
$\widetilde{Re}_{\theta t}$	local transition onset momentum thickness Reynolds number (transported quantity)
Re_ν	vorticity Reynolds number, Sy^2/ν
$u,\ v,\ w$	velocity components
$x,\ y,\ z$	Cartesian coordinates
P	production term of transport equation
E	destruction term of transport equation
S	strain rate magnitude
U	local velocity
Tu	turbulence intensity [in %]
Greek symbols	
γ	intermittency
θ	boundary layer momentum thickness
ν	kinematic fluid viscosity
τ_{ij}	Reynolds stress tensor
ω	specific turbulence-dissipation rate
Ω	vorticity magnitude
σ_f	γ-transport equation diffusion coefficient
$\sigma_{\theta t}$	$\widetilde{Re}_{\theta t}$ -transport equation diffusion coefficient
λ_θ	pressure gradient parameter
Subscript	
l	laminar
t	transition onset
T	turbulent
∞	freestream
onset	onset of transition
θt	momentum thickness at transition onset